

***XMM-Newton* and optical observations of the eclipsing polar CSS081231:071126+440405[★]**

H. Worpel, A. D. Schwope

Leibniz-Institut für Astrophysik Potsdam (AIP), An der Sternwarte 16, 14482 Potsdam, Germany

September 28, 2015

ABSTRACT

Aims. We aim to study the temporal and spectral behaviour of the eclipsing polar CSS081231:071126+440405 from the infrared to the X-ray regimes.

Methods. We obtained phase-resolved *XMM-Newton* X-ray observations on two occasions in 2012 and 2013 in different states of accretion. In 2013 the *XMM-Newton* X-ray and UV data were complemented by optical photometric and spectroscopic observations.

Results. CSS081231 displays two-pole accretion in the high state. The magnetic fields of the two poles are 36 and 69 MG, indicating a non-dipolar field geometry. The X-ray spectrum of the main accreting pole with the lower field comprises a hot thermal component from the cooling accretion plasma, kT_{plas} of a few tens of keV, and a much less luminous blackbody-like component from the accretion area with $kT_{\text{bb}} \sim 50\text{--}100$ eV. The high-field pole, which was located opposite to the mass-donating star, accretes at a low rate and has a plasma temperature of about 4 keV. On both occasions the X-ray eclipse midpoint precedes the optical eclipse midpoint by 3.2 seconds. The centre of the X-ray bright phase shows accretion-rate-dependent longitudinal motion of ~ 20 degrees.

Conclusions. CSS081231 is a bright polar that escaped detection in the RASS survey because it was in a low accretion state. Even in the high state it lacks the prominent soft component previously thought to be ubiquitous in polars. Such an excess may still be present in the unobserved extreme ultraviolet. All polars discovered in the *XMM-Newton* era lack the prominent soft component. The intrinsic spectral energy distribution of polars still awaits characterisation by future X-ray surveys such as eROSITA. The trajectory taken by material to reach the second pole is still uncertain.

Key words. stars: individual: CSS081231:071126+440405 – stars: cataclysmic variables – binaries: eclipsing – X-rays: stars

1. Introduction

Polars, also known as AM Herculis stars, are accreting binary systems in which material is transferred via Roche lobe overflow from a dwarf star onto a strongly magnetic white dwarf (WD). In these cataclysmic variable (CV) systems, no accretion disc forms because the WD's magnetic field is strong enough to cause the material lost by the secondary to travel down the magnetic field lines directly onto the magnetic poles. These systems are important for understanding accretion processes in the presence of a powerful magnetic field.

An identifying characteristic of polars has historically been their prominent soft X-ray emission. This property led to the discovery of numerous polars with the EINSTEIN, EXOSAT, ROSAT, and EUVE satellites. However, *XMM-Newton* observations of X-ray selected polars (e.g. Ramsay & Cropper 2004) and the discovery of new polar systems reveal growing evidence that a soft X-ray component is not present in the majority of polars.

CSS081231:071126+440405, henceforth J071126, is a polar discovered on 2008 December 31 by the Catalina Sky Survey (Drake et al. 2009; Templeton et al. 2009), when it suddenly brightened by over three magnitudes. It had been observed previously, but not recognised as a variable star. It is an eclipsing system with a period of 7031 seconds and an optical eclipse duration of 433.08 seconds (Schwope et al. 2015; hereafter S+15).

Eclipses in polars benefit the observer because the viewing geometry is constrained through knowledge of the inclination, and the periodic obscuration of different sites in the system allows the contributions to the total flux from the different emission sites to be distinguished. Additionally, if there are any circumbinary planets, they can be detected by the Rømer delay of the eclipse (e.g. Schwarz et al. 2009; Qian et al. 2011; Schwope & Thinius 2014 for the case of HU Aquarii).

S+15 compiled a data set of optical observations of J071126 covering a time span of 5.3 years. They used the data to obtain a precise linear ephemeris for the eclipse midpoints, finding no evidence of any deviations from it, which is a result that sets a tentative upper limit on the mass of a circumbinary planetary companion of two Jupiter masses.

S+15 were unable to find a binary system accretion geometry that satisfied all of their observational constraints. Though the high and intermediate accretion states can be explained by a colatitude and azimuth of the magnetic axis of $\beta = 18^\circ$ and $\psi = -3^\circ$, and a system inclination of $i = 79.3^\circ - 83.7^\circ$, the location of the accretion spot in the low state ($\psi \approx 10^\circ$) is not consistent with these parameters. The authors postulated a non-dipolar field structure as a possible solution.

Observations of J071126 in ultraviolet and X-rays may help uncover the accretion geometry. We present a study of two *XMM-Newton* observations of the source, taken one year apart, of J071126 in a high state (2013) and a state of reduced accretion (2012). The observation in 2013 was accompanied by four nights of photometric observations with the STELLA robotic telescope

[★] Based on observations obtained with XMM-Newton, an ESA science mission with instruments and contributions directly funded by ESA Member States and NASA

(Strassmeier et al. 2004), and two nights of low-resolution spectroscopy at Calar Alto.

In Sect. 2 we give the details of our data reduction and analysis methods. Sect. 3 contains our results, and in Sect. 4 we discuss the possible accretion scenario at the two magnetic poles.

2. Observations and data reduction

2.1. XMM-Newton X-ray and ultraviolet observations

The *XMM-Newton* satellite made two observations of J071126. The first of these (henceforth Obs1) was made on 2012 April 10 (observation ID 0675230101) and lasted ~ 32 ks. The second (Obs2) was made on 2013 April 8 (observation ID 0693580101) and lasted ~ 24 ks. The observations thus covered 4.59 and 3.42 cycles of the 1.95 hour binary. The EPIC-*pn* and -MOS cameras were operated in full frame mode with the thin filter in both observations. *XMM-Newton* observed the star simultaneously with the Optical Monitor (OM) in fast mode with the UVM2 and UVM1 filters for both observations. The UVM2 and UVM1 filters have effective wavelengths of 2310 Å and 2910 Å, respectively (Kirsch et al. 2004a). In Obs1 a total of 1 3197 s of UVM1 data and 1 5834.5 s of UVM2 data are available. In Obs2 we have 7 678 s and 14 169.5 s of data in those filters. We have not used the RGS because of low signal-to-noise.

The raw data were reduced using the *XMM-Newton* Science Analysis System (SAS) version 14.0.0. The EPIC-*pn* and MOS data were processed with the standard tasks *epchain* and *emchain* to generate calibrated event lists. The *epreject* task was run for EPIC-*pn* data. All timing data in this work were corrected to the solar system barycentre using the SAS *barycen* task. The photon lists were filtered to only include photons with energies between 0.15 keV and 12.0 keV for the MOS instruments and between 0.15 keV and 15.0 keV for the EPIC-*pn* instrument. For the analysis of hardness ratios and spectra we restricted the energies further (see subsequent sections). For each photon arrival time we additionally assigned an orbital phase in the range $\phi \in [0, 1)$ according to the ephemeris in S+15. Background-subtracted light curves were produced with the *epicccorr* task to correct for vignetting, bad pixels, etc. The OM data were reduced using the *omfchain* task.

Our source extraction regions were circles centred on the source, where the precise location of the source was determined with the SAS *edetectchain* task and the best extraction radius found with the *eregionanalyse* task. The source extraction radii were in the range 20 to 28 arcseconds, with enclosed energy fractions of over 90% in each case. The background extraction regions were boxes lying as near the source as was practical, with care taken to ensure approximately the same CCD readout time. We excluded a circular area of radius 42.5 arcseconds, centred on the source, from the background-extraction region.

2.2. Optical photometry

J071126 was observed with the robotic telescope STELLA during four nights in 2013 April. The overall settings, the data reduction and analysis, and the mean light curve have already been presented in S+15. We compared the relative flux between our target and the comparison star #139 of the American Association of Variable Star Observers (AAVSO) sequence. The AAVSO gives a Henden sequence for this star with $B = 14.696$ and $V = 13.918$. STELLA observations were obtained through an SDSS *g* filter. The equation given by Bilir et al. (2005) was used to transform to the SDSS system, $g_{\#139} = 14.3$.

STELLA observations were performed on the nights of April 1, 7, 10, and 12. Full phase coverage was achieved on each occasion. The optical observations that happened closest to the *XMM-Newton* observations began on April 7 and covered orbital phases 19135.20 – 19137.91, so only a few cycles earlier than the X-ray observations beginning in cycle 19144.

2.3. Optical low-resolution spectroscopy

Low-resolution spectroscopy was performed during the nights of 2013 March 20 and March 21 with the 2.2m telescope of the Calar Alto observatory. It was equipped with CAFOS, a grism spectrograph and imager. The B400 grism provided a wavelength coverage from 3360 – 9650 Å at a FWHM resolution of 9.7 Å as measured from calibration lamp spectra. The integration time per spectrum was 3 m. The time resolution thus achieved was 243 s (0.035 phase units). On both nights 19 spectra were taken, but clouds at the end of the second observation degraded the quality of the spectra considerably. The spectroscopic observations covered the binary cycles 18913.96 – 18914.62 and 18925.59 – 18926.18. Although these observations were a few weeks earlier than the STELLA and *XMM-Newton* observations, the bottom panel of Fig. 7 shows that J071126 was similarly bright in the optical on both occasions. We are therefore confident that we are comparing similar accretion states.

The spectrograph was rotated so that comparison star #142 from the AAVSO chart could be observed simultaneously. This star at RA2000 = 7:11:35.5, DE2000 = 44:04:03.3 has $B = 15.167$, $V = 14.158$, $Rc = 13.621$, $Ic = 13.109$.

Arc lamp spectra (Hg+He+Rb) for wavelength calibration were obtained before and after the sequence of the target star. No spectrophotometric standard star was observed during those two nights through the same grisms. To achieve a rough spectrophotometric calibration, standard star observations were sought in the data archive at Calar Alto. We found two standard star observations with the same instrumental setup. The two spectral response curves, based on observations of the standard stars BD+28_4211 observed in May 2010 and HZ44 observed in March 2008, differed by a factor of almost 2 in absolute flux but showed a similar shape. The response curves were thus used to put the target spectra on a relative scale.

To achieve a proper photometric calibration and to put the spectra on an absolute scale the data of the comparison star #142 were used. Firstly, an achromatic correction with the mean brightness of the comparison star in the wavelength interval 5000 – 7000 Å was applied to the spectra of both the target star and the comparison star. This procedure accounted for seeing and transparency variations. Secondly the average spectrum of the comparison star was folded through the BVRcIc filter curves and correction factors determined at the corresponding central wavelengths of the filters. The factors were then fitted with a polynomial of degree 2 and the correction function was applied to all spectra of the target. The correction function is not fully determined at the blue and red ends of the spectrum owing to the lack of sampling points. Given the uncertainties of the various reduction steps, we estimate a photometric accuracy of our final spectra of about 15% in the centre and of 30% at the end of the spectral range covered with the B400 grism.

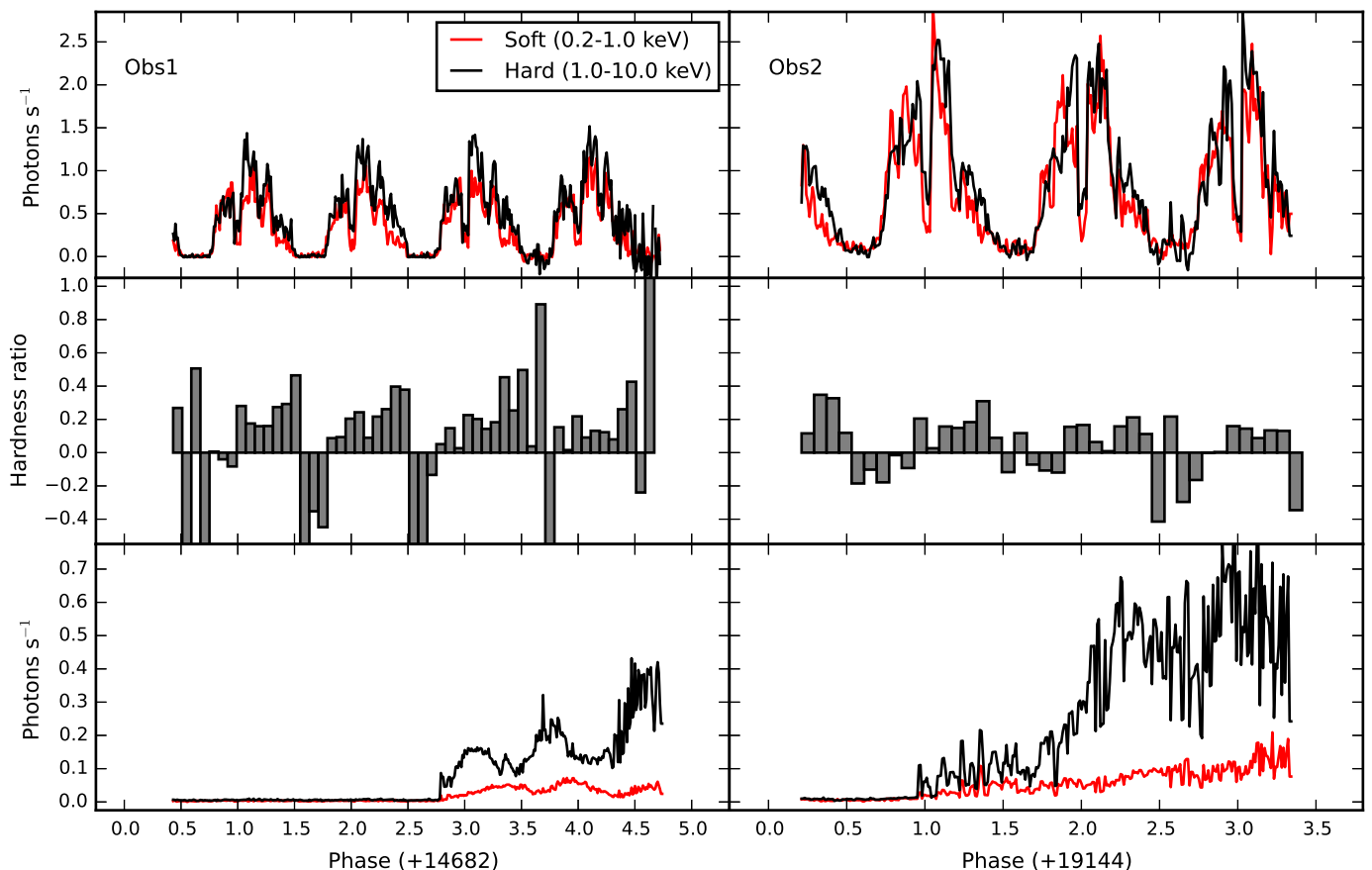


Fig. 1. X-ray light curves of J071126 in both observations, and stacking data for the EPIC-MOS1, MOS2, and *pn* instruments. Top panels show background-subtracted source light curves in soft and hard X-rays. The middle panels show hardness ratios (Eq. 1). Bottom panels show exposure-corrected background light curves. The light curves have been binned into 100 bins per cycle (70.3 s). The count rates for the top two panels have been corrected for the enclosed count fraction of the source extraction regions, but we have not corrected for data gaps in EPIC-*pn*. Two dips are visible in each of the first two cycles of Obs2 in soft X-rays.

3. Analysis and results

3.1. X-ray light curves

Figure 1 shows the X-ray light curves of the two observations. As is typical of eclipsing polars, the light curves are dominated by the emission from a self-eclipsing accreting pole, interrupted by a short period of very low flux when the WD and main accreting pole are eclipsed by the secondary star. The X-ray flux is larger in the second observation, indicating a higher accretion rate. The bottom two panels of Fig. 1 show the background flux. Soft proton flares begin to affect both observations about half way through, and Obs2 is more severely affected.

Phase-folded light curves are shown in Fig. 2. The shape of the light curves suggests that the bright phases have shifted in longitude between Obs1 and Obs2. To verify this observation, we found the centres of the bright phases as follows. We binned the data into 100 bins per phase. We defined the peak count rate of the bright phase as the mean of the brightest three points in each cycle, for each instrument, and took the rise and fall of the bright phase to be the times at which the count rates reached or dropped below 20% of the peak count rate. Taking unweighted averages for each cycle, we found the bright phases were centred at $\phi_c = 0.035 \pm 0.003$ and $\phi_c = -0.031 \pm 0.006$ for Obs1 and Obs2.

This result shows that the midpoint of the bright phase is indeed earlier in Obs2 than in Obs1. These bright phase mid-

points correspond to a trailing longitude of $\psi \approx -11 \pm 2^\circ$ in Obs1 and a leading spot longitude of $\psi \approx 12 \pm 1^\circ$ in Obs2. Some care should be taken in interpreting these numbers because the bright phase is asymmetrically shaped, and therefore the exact midpoint can depend on what count rate is taken to mark its rise and fall. Nonetheless, the motion of the bright spot between observations is qualitatively similar to the accretion-rate dependent motion found for this source in optical light curves in S+15.

There is a slight indication in Fig. 2 of an increase in X-rays around phase $\phi \approx 0.5$ in Obs2, suggesting a second accreting pole. We discuss this secondary hump in Sect. 3.4.

We have also analysed hardness ratios in X-rays for both observations:

$$HR = (H - S)/(H + S), \quad (1)$$

where H and S are the background-corrected count rates in the 1.0-10.0 keV energy band and the 0.2-1.0 keV energy band. The choice of non-standard bands for the hardness ratio was motivated by the presence of two radiation components in the soft X-ray regime below 1 keV and a hard thermal spectrum above this energy (see Sect. 3.3.1). The results are shown in the middle panels of Fig. 1. For Obs1 the hardness ratio is around $HR \approx 0.2$ for the bright phase and much softer in the faint phase, and there is slight evidence that the bright phase has a rising hardness profile. In Obs2, the bright phase has a hardness ratio of 0.1, and the faint phase is also softer.

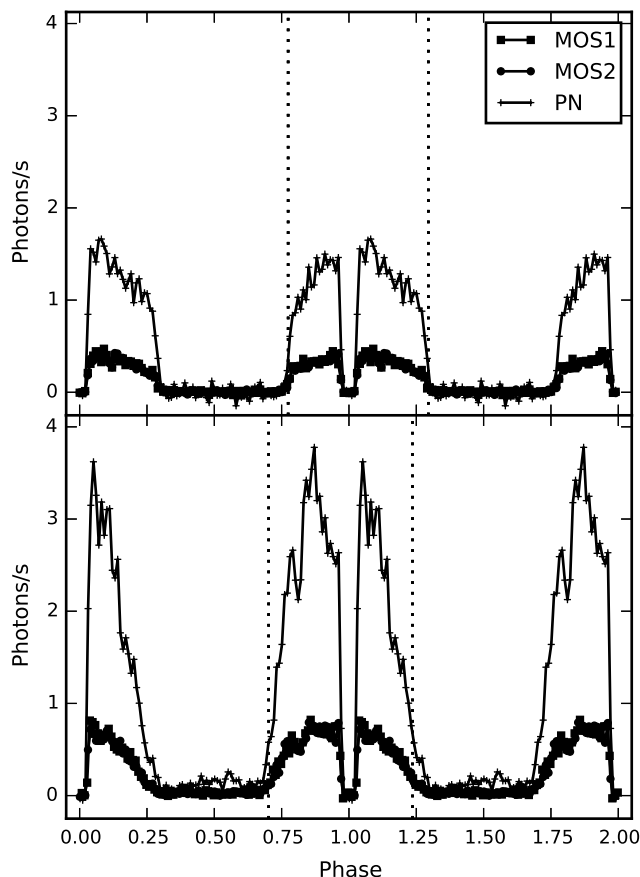


Fig. 2. Phase-folded X-ray light curves of J071126 in both observations, for the EPIC-MOS1, MOS2, and *pn* instruments. The light curves have been binned into 100 bins per cycle, and two phases are plotted for clarity. The energy ranges are 0.2–12 keV for the EPIC-MOS instruments and 0.2–15 keV for EPIC-*pn*, and count rates have been corrected for the enclosed count fraction of the source extraction regions. Dotted vertical lines indicate the beginning and end of the bright phase, clearly showing the longitudinal shift.

The soft X-rays from the first two cycles of Obs2 are shown in Fig. 3. Aside from the eclipse, two features are evident: a dip at phases 0.81 and 0.83 (the *bright phase dip*) and another just before eclipse ingress (the *pre-eclipse dip*). Both bright phase dips have been observed previously in, for example, HU Aqr (Schwope et al. 2001), but in this source they are narrower and occur later in phase. The bright phase dip was previously found in optical for this source by Katysheva & Shugarov (2012). Both features have higher hardness ratios than the rest of the bright phase, suggesting that they arise from absorption, which primarily affects the low energy end of the X-ray spectrum. It also seems that the bright phases have a rising hardness ratio profile in both observations.

We applied the Bayesian Block method (Scargle 1998; Scargle et al. 2013) to determine the starts and ends of the eclipses; see also Schwope et al. (2002) for an earlier application of this algorithm to CV eclipse timing. Because we need to perform background subtraction, with the data degraded by soft proton flares that affect the second half of both observations, we have used the weighted-photon adaptation to the original algorithm described in Worpel & Schwope (2015). We produced Bayesian Block representations for all instruments but only EPIC-*pn* data were used for the timings because the EPIC-MOS

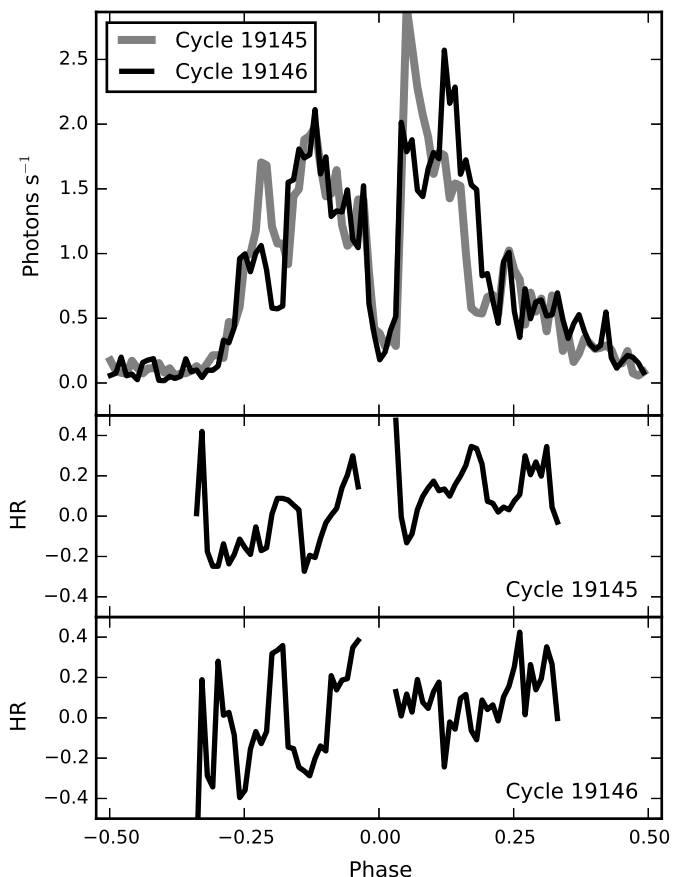


Fig. 3. Cycles 19145 and 19146 (Obs2) in soft (0.2–1.0 keV) X-rays (top panel). Bright phase dips occurring at phase 0.81 – 0.83 and pre-eclipse dips beginning at about phase 0.9 and leading into ingress are visible. The middle and bottom panels show hardness ratios (Eq. 1) for these two cycles. The two dips are much harder than the rest of the bright phase. For clarity the eclipses and faint phases are not plotted in the hardness ratio panels. The third cycle of Obs2 is omitted because it is severely affected by data gaps.

data is accurate to only 2.6 s in full-frame mode. The EPIC-*pn* instrument has a timing resolution of 0.0734 s (Kirsch et al. 2004b). The Bayesian Block light curves are shown in Fig. 4. These do not contain corrections for vignetting, bad pixels, etc. which for normal light curves would be performed by the *epiclc-corr* task. This is why the count rate appears lower. The eclipse parameters are given in Table 2. Uncertainties on a Bayesian Block change point was determined by generating many simulated sequences of photon arrival times with the same count rates as the blocks the change point separates, for source region and background region photons. The third cycle of Obs2 is affected by periodic data gaps in EPIC-*pn* data because the total count rate exceeds telemetry limits (see *XMM-Newton Users Handbook*, Sect. 4.3.1). The data gaps begin in the fall of the second bright phase and prevent accurate eclipse timing for the third eclipse, so for the third eclipse we used EPIC-MOS2 data, which are unaffected but have poorer timing resolution.

3.2. Multifrequency light curves

The OM light curves (see Figs. 5 and 6) are qualitatively similar to the X-ray light curves. In both observations the accretion spot is plainly visible as a bright phase, which is interrupted by a deep

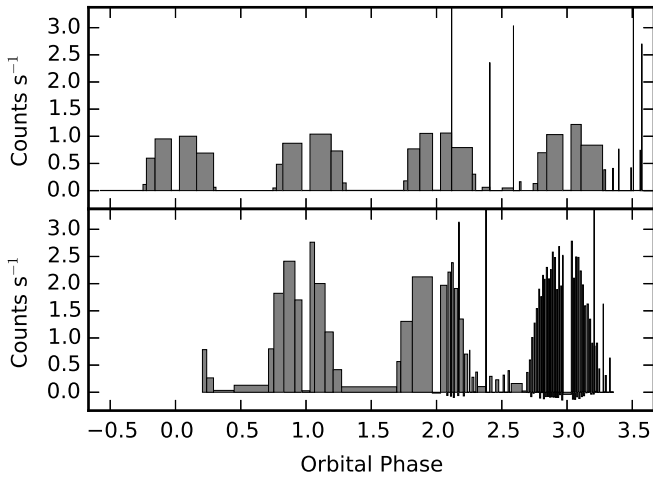


Fig. 4. Bayesian Block light curves of Obs1 and Obs2. The eclipses are clearly defined, except for the third eclipse of Obs2, which is affected by data gaps. The gaps are plainly visible, beginning around phase 2.1. A few noisy blocks of implausible count rate are also visible (see Worpel & Schwope 2015) but do not affect the eclipse timings.

eclipse. In Obs1, the bright phase is symmetrical and flat-topped. There are no visible changes in its shape over two orbital cycles in either filter. In Obs2 the bright phase has a sharp rise and slow decline in both filters, though the rise is visibly slower in the UVM2 filter. Additionally, in Obs2 there is a small secondary hump at phase $\phi \approx 0.55$, but only in the softer filter. There is no evidence of this in the UVM2 data, but this may simply be due to the lower sensitivity of that filter. The secondary hump also has a fast rise and slow decline, extending from about $\phi = 0.45$ to $\phi = 0.65$, but determining its end is difficult because of a data interruption during the UVW1 observation.

There is no evidence of any pre-eclipse or bright phase dips in either observation. This is surprising, since the features were present in soft X-rays in Obs2. Even a low N_H column density of $5 \times 10^{20} \text{ cm}^{-2}$ (see Sect. 3.1) would cause a factor 2 extinction at 2500 \AA , assuming the absorption properties of local absorbing material is similar to interstellar material. However, in this part of the spectrum absorption is dominated by free-free absorption and the optical depth is proportional to the square of the column density (Watson et al. 1989, 1990). Thus even a slightly lower N_H would result in a much more subdued dip feature.

As with the X-ray hardness ratios, there is clear evidence of a phase dependence on the UV hardness ratio. The bright phase is softer than the faint phase in both observations, opposite to the behaviour in X-rays. The secondary hump in Obs2 is also softer in UV than the faint phase. Only the qualitative behaviour of the hardness ratio is relevant, not the values themselves, because of the different transmission properties of the UVW1 and UVM2 filters.

The midpoint of the bright phase moves from a trailing longitude in Obs1 to a leading longitude in Obs2, similar to the behaviour of the bright phase in X-rays. Taking the rise and fall of the bright phase to be 20% brighter than the mean faint phase brightness, and stacking the phase-folded light curves and excluding the secondary hump in Obs2, we found a trailing spot longitude of $\psi \approx -10^\circ$ in Obs1 and a leading spot longitude of $\psi \approx 10^\circ$ in Obs2.

J071126 was gradually becoming brighter by some 60% in the first half of 2013 April as revealed through our

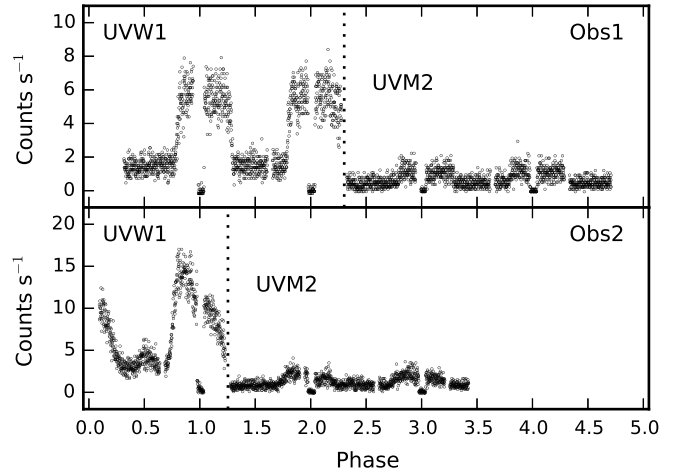


Fig. 5. Optical monitor light curves for the two observations as a function of orbital phase. The binning is 10 s. For both Obs1 and Obs2 the filters were changed from UVW1 to UVM2 midway through the observation, as indicated by the dotted vertical lines.

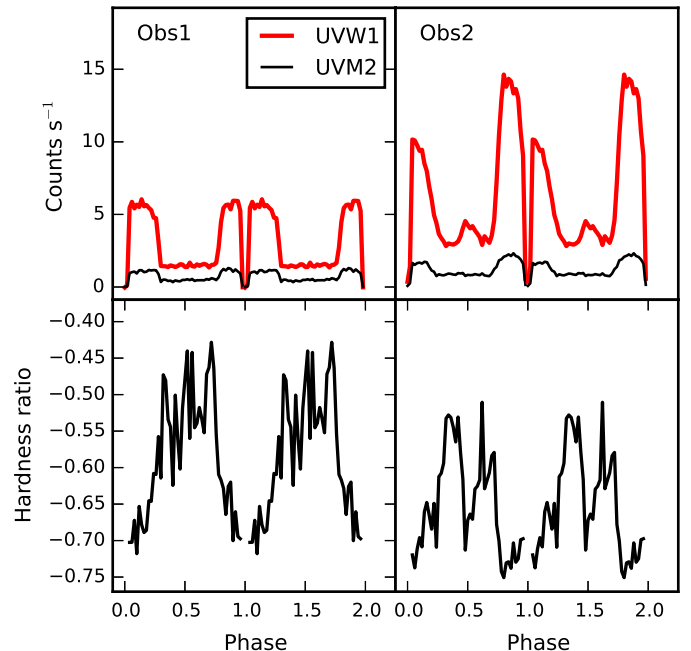


Fig. 6. Phase-folded optical monitor light curves (top panels) and hardness ratios (bottom panels). The secondary hump in Obs2 is visible in UVW1, but is not apparent in UVM2. The bright phase is much softer than the faint phase, as is the secondary hump. Obs2 is generally slightly softer than Obs1.

STELLA/WiFSIP monitoring. Mean g-band magnitudes in the bright ($\phi = 0.89 - 0.93$) and faint ($\phi = 0.31 - 0.35$) phases were found to be 15.12, 15.10, 14.94, 14.64 and 17.15, 17.14, 16.92, 16.66 on April 1, 7, 10, and 12, respectively. On all occasions there was a steeper increase towards the orbital maximum and a slower decline. There was a shoulder on the decreasing branch of the light curve at orbital phase 0.27. On April 12, when the source appeared brightest, further shoulders occurred at phases 0.75 and 0.21, that might indicate that the source develops further emission regions.

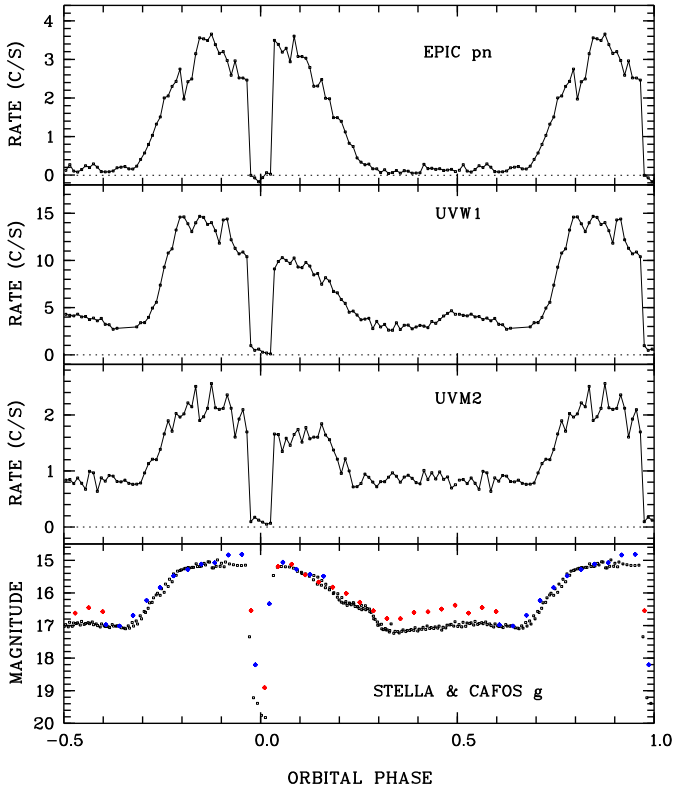


Fig. 7. Phase-folded X-ray, ultraviolet and optical data obtained 2013 March & April. The bin size is 0.01 phase units (70.3 s) in the three upper panels. The optical data shown in the lowest panel shows STELLA data (60 s bin size) obtained on the night of April 7/8 and light curves obtained from the low-resolution optical spectroscopy with CAFOS (red: March 20, blue March 21; 243 s bin size).

All multi-wavelength light curves obtained in 2013 April, which are averaged into 100 phase bins, are displayed in Fig. 7. All have the asymmetric shape in common, reaching maximum brightness during the first half of the bright hump. The X-ray light curve appears to be the most symmetric of the four light curves shown. The steep increase and the slower decline of the low-energy light curves is likely due to the optical thickness effects of the cyclotron component. The lowest panel also includes g-band data from the CAFOS spectroscopy in March 2013.

3.3. The main orbital hump

3.3.1. X-ray spectroscopy

During both observation X-ray spectra were extracted using the bright phase intervals, which were identified by visual inspection of the Bayesian Block light curves, and excluding the eclipses. We analysed the X-ray spectra using version 12.8.2p of the XSPEC software package (Arnaud 1996; Dorman & Arnaud 2001). During spectral fitting the EPIC-*pn* and EPIC-MOS data were analysed simultaneously in an energy range of 0.2–10.0 keV for EPIC-*pn* and 0.2–8.0 keV for EPIC-MOS. To accommodate bins with low photon counts, we used Churazov weighting (Churazov et al. 1996).

We initially fit the data for both observations using a single MEKAL plasma model (Mewe et al. 1985; Liedahl et al. 1995), with the metal plasma abundances frozen at solar values and redshift at zero. These fits did not give good χ^2_ν values. Visual inspection of the fits showed that the major cause of the poor χ^2_ν

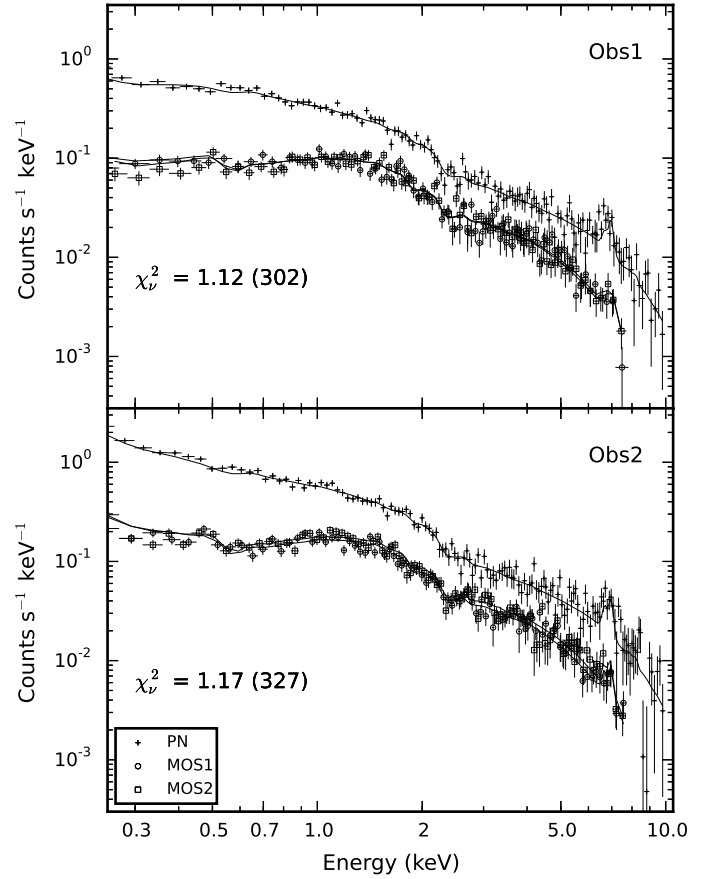


Fig. 8. Simultaneous fits to EPIC-*pn* and EPIC-MOS spectra of the bright phase of both observations. The data are shown as points with error bars, and the fit to the data is represented by solid black lines. The spectra are well fitted by the MEKAL+*bbodyrad* model.

values was an excess of photons at low energies. To correct this, we fitted the data again with the sum of a MEKAL component and a soft blackbody. These fits gave adequate χ^2_ν . The spectral parameters are given in Table 1. For a distance of 390 pc, the soft blackbody in Obs2 would represent a sphere of radius 510 km. This value is plausible, since it is much smaller than the radius of the WD itself.

The uncertainties on the plasma temperature were found using XSPEC's *steppar* command to achieve a confidence interval of 99%. Uncertainties on fluxes for all models were calculated using the *cflux* convolution component. The uncertainties in the fluxes are often proportionally smaller than those on the temperatures and normalisations because these two parameters vary independently. The spectral fits are shown in Fig. 8. The necessity of adding a second component to the low-energy end suggests that N_H absorption is likely to be small. We confirmed this result by adding a *tbabs* multiplicative component to the MEKAL+*bbodyrad* model and repeating the fits. We obtained an N_H value consistent with zero and no improvement in χ^2_ν .

We determined upper limits on N_H by increasing it until no statistically acceptable fit could be obtained, to 99% confidence. This upper limit was $0.135 \times 10^{22} \text{ cm}^{-2}$ for Obs1 and $0.081 \times 10^{22} \text{ cm}^{-2}$ for Obs2. We found maximum unabsorbed fluxes for the MEKAL and blackbody components by freezing N_H at its upper limits, and the other spectral component parameters to their previously determined values, and fitting again. The upper limits to the fluxes for the MEKAL component were

$4.2 \times 10^{-12} \text{ erg s}^{-1} \text{ cm}^{-2}$ in Obs1 and $6.8 \times 10^{-12} \text{ erg s}^{-1} \text{ cm}^{-2}$ in Obs2. For the blackbody component the maximum fluxes were $3.6 \times 10^{-12} \text{ erg s}^{-1} \text{ cm}^{-2}$ in Obs1 and $6.1 \times 10^{-12} \text{ erg s}^{-1} \text{ cm}^{-2}$ in Obs2.

To estimate the amount of absorption in the two dip features we returned to the MEKAL+*bbodyrad* model in Table 1 and added a *tbabs* absorption coefficient to determine the N_H needed to produce a given reduction in flux between 0.2 and 1.0 keV. We required 1.4×10^{20} , 4.3×10^{20} , and $1.4 \times 10^{21} \text{ atoms cm}^{-2}$ to achieve reductions in flux of 25%, 50%, and 75%. We have selected a range of flux reduction factors because the actual depths of the dips is difficult to estimate. Similar column depths have previously been reported for pre-eclipse dips in HU Aqr (Schwarz et al. 2009).

Inspection of the spectral fits in Fig. 8 suggests the possible presence of a fluorescent iron line at 6.4 keV, based on four or five bins of positive residuals. We estimated the equivalent width of the possible iron line as follows. We took the MEKAL + *bbodyrad* model with the parameters of Table 1 frozen, and restricted the energy range to 5.0–8.0 keV to isolate the emission line complex. Even in this energy range, the model is statistically acceptable. We added a Gaussian emission line with energy frozen at 6.4 keV, but with width and normalisation allowed to vary, and fitted the spectrum again. The fits suggest an equivalent width, using XSPEC’s *eqwidth* command, of 100–150 eV in both observations. We then increased the normalisation of the Gaussian until the fit was no longer statistically acceptable (to 99% confidence), giving an upper limit of about 500 eV in both observations. These numbers are consistent with the results of Ezuka & Ishida (1999), who found poorly constrained equivalent widths of similar magnitude for several polars using ASCA data. We emphasize, however, that the evidence of the line being there at all is not strong.

To quantify any possible effect of the proton flares on the spectral fits, we extracted bright phase spectra for all instruments in each orbital cycle separately and compared them to the corresponding model in Table 1. The four cycles of Obs1 gave χ^2_ν of 1.11, 1.08, 0.96, and 1.06. In Obs2 we obtained χ^2_ν of 1.70, 1.94, and 1.16, but the poor results for the first two could be remedied by allowing the temperature of the blackbody component to vary by $\sim 10 \text{ eV}$. Since the proton flare is strongest at high energies (Fig. 1), it is likely that this result represents a definite variation in the soft component of the spectrum. There is therefore no evidence that background subtraction of the soft proton flare is inadequate even for periods of strong flaring. We have therefore also not extracted good time intervals.

3.3.2. Optical spectroscopy

Optical spectra representing the minimum phase and the maximum phase are displayed in Fig. 9. They show the typical emission line spectrum of polars in their high states with H-Balmer, HeI and HeII emission. The minimum spectrum shows a flat continuum, while the continuum in the bright phase is very blue with a maximum intensity outside the spectral range covered here. The continuum does not show a completely smooth variation, and in particular the spectrum taken during the rise to and fall from the bright phase shows undulations that are reminiscent of cyclotron harmonics.

The harmonics offer the opportunity to measure the field strength in the main accretion region. To extract the cyclotron harmonic lines from the main pole, we first subtracted the main emission lines from each spectrum by fitting Gaussians interactively. We then subtracted the spectrum obtained at minimum

Table 1. Spectral fit parameters and their uncertainties, fit statistics, and model bolometric fluxes for the bright phase in both observations. Question marks in the upper or lower uncertainties indicate that no constraint could be determined. Normalisations for the MEKAL model are given in units of $10^{-14} \int n_e n_H dV / 4\pi [D_A(1+z)]^2$, where D_A is the angular diameter of the source, and n_H, n_e are hydrogen and electron densities. Normalisations for the blackbody model are in units of $(R/D_{10})^2$ where R is the radius of the object in kilometers and D_{10} is its distance in units of 10 kpc. All fluxes are calculated in the energy range $10^{-6} - 100.0 \text{ keV}$. This energy range is wide enough that small changes in the upper and lower limits do not change the results. Uncertainties are given at the 99% confidence level.

MEKAL+BBDYRAD, 0.2–10.0 keV		
	Obs1	Obs2
$kT_{\text{mekal}} \text{ (keV)}$	$17.0^{+6.6}_{-4.0}$	$14.1^{+3.7}_{-2.4}$
$\text{norm}_{\text{mekal}} (10^{-3})$	$1.49^{+0.08}_{-0.06}$	$2.49^{+0.11}_{-0.08}$
$kT_{\text{bb}} \text{ (keV)}$	$0.09^{+0.03}_{-0.03}$	$0.05^{+0.01}_{-0.01}$
norm_{bb}	175^{+1900}_{-125}	13000^{+18000}_{-7000}
$\chi^2_\nu \text{ (dof)}$	1.12 (302)	1.17 (327)
$\text{Flux} (10^{-12} \text{ erg s}^{-1} \text{ cm}^{-2})$	$3.86^{+0.08}_{-0.08}$	$8.10^{+0.15}_{-0.15}$
$\text{Flux}_{\text{mekal}} (10^{-12} \text{ erg s}^{-1} \text{ cm}^{-2})$	$3.73^{+0.08}_{-0.08}$	$6.23^{+0.13}_{-0.13}$
$\text{Flux}_{\text{bb}} (10^{-12} \text{ erg s}^{-1} \text{ cm}^{-2})$	$0.13^{+0.03}_{-0.03}$	$1.27^{+0.12}_{-0.12}$

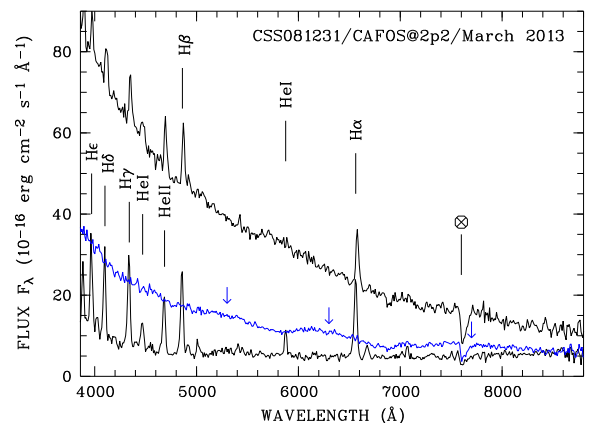


Fig. 9. CAFOS spectra obtained during bright ($\phi = 0.92 - 0.95$) and faint phases ($\phi = 0.31 - 0.37$) a few weeks prior to Obs2. The spectrum displayed in blue was obtained at phase 0.18 with atomic emission lines subtracted. It shows modulations that were identified with cyclotron harmonics indicated by arrows. Hydrogen Balmer, HeI, and HeII lines are prominent. The feature indicated with a cross is an atmospheric line; the spectra have not been corrected for them.

phase from the spectrum at fall phase and fitted a low-order polynomial to the difference, representing the continuum. After subtracting this continuum one is left with a spectrum that is modulated by cyclotron harmonic lines and noise. The cyclotron harmonics are centred on 5200, 6300, and 7700 Å and can be reproduced with an isothermal cyclotron model assuming $kT = 5 \text{ keV}$ and $B_1 = 36 \text{ MG}$ (Fig. 10) using the models in a series of papers (see e.g. Campbell et al. 2008; Schwope et al. 2003, and references therein).

Cyclotron harmonic humps could be recognised only during the rise and fall of the bright phase but not in its central part. Interestingly, the cyclotron humps seem to be shifted as a function of phase. They are most blueshifted at the beginning

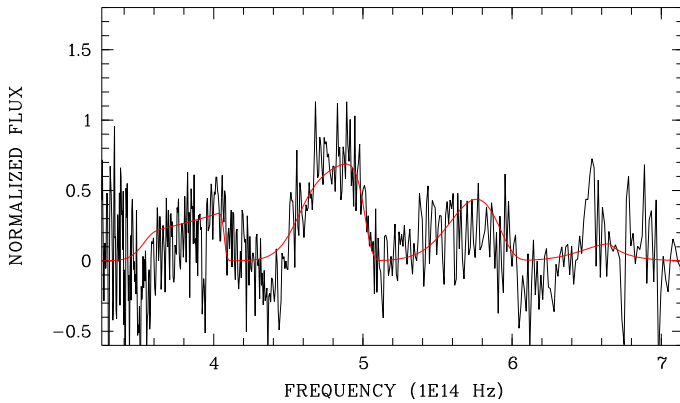


Fig. 10. Continuum-subtracted cyclotron humps observed at phase 0.18 with a cyclotron model for 36 MG superposed

and end of the bright phase and become redshifted during the bright phase, when the line of sight comes closer to the magnetic axis in the accretion spot. This is opposite to what is observed in other polars where the highest redshift was observed when the accretion spot was approaching the limb of the WD (see e.g. Schwöpe et al. 2003; Burwitz et al. 1996, for the cases of HU Aqr and RX J0453.4–4213), and it is contrary to what is expected for plasma emission from a point-like, isothermal accretion region. As a result, this observation could be evidence of an extended cyclotron-emitting region with successively self-eclipsing parts belonging to regions of slightly different field strengths. A mixture of different field strengths would manifest as a blurring of the cyclotron harmonics (e.g. Schwöpe et al. 1990), but our spectroscopic data do not have high enough quality to investigate this effect.

The flux in the cyclotron component is difficult to determine from optical observations alone since it peaks shortward of the spectral range covered by our low-resolution spectroscopy. The similarity of the optical and ultraviolet light curves suggests they are formed by the same emission process, predominantly cyclotron radiation. Photospheric radiation from the heated region around the accretion spot might also be present, but seems to be a minor contributor in this case, since photospheric radiation typically gives symmetric light curves (e.g. Gänsicke et al. 1998). The bright-phase peak flux in the optical (at 3500 Å) was $8.5 \times 10^{-15} \text{ erg cm}^{-2} \text{ s}^{-1} \text{ Å}^{-1}$ (corrected for the faint-phase contribution) whereas it was $(5.2 \pm 0.5) \times 10^{-15} \text{ erg cm}^{-2} \text{ s}^{-1} \text{ Å}^{-1}$ and $(3.1 \pm 0.5) \times 10^{-15} \text{ erg cm}^{-2} \text{ s}^{-1} \text{ Å}^{-1}$ in the UV at 2910 Å and 2310 Å, respectively. The optical-UV SED therefore shows a peak at about 3300 Å that steeply decreases towards the UV and the optical. The shape is not compatible with a hot photospheric spectrum from the WD but is consistent with one dominated by cyclotron radiation. The bolometric flux in this component is $F_{\text{cyc}} \simeq 2.2 \times 10^{-11} \text{ erg cm}^{-2} \text{ s}^{-1}$, so roughly three times more luminous than the X-ray plasma component.

3.4. Optical and X-ray spectroscopy of the secondary orbital hump

Optical light curves have occasionally shown a secondary hump centred on phase 0.50–0.60, as described in S+15. This feature is also present in the data obtained with the OM (see Sect. 3.2) between phases 0.45 and 0.65 in the UVW1 filter. The secondary hump is also visible in the g-band STELLA light curves, as well as in the CAFOS photometry (see Fig. 7). The feature remained

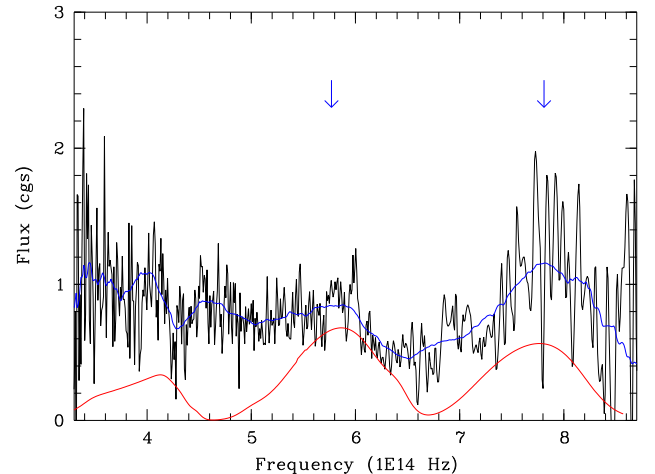


Fig. 11. Mean faint phase spectrum ($\phi = 0.38 - 0.60$) after subtracting atomic emission lines and the mean spectrum of the phase interval 0.31–0.37. The blue line is a boxcar-smoothed version of the same data. The arrows indicate tentatively identified cyclotron harmonics. The red line is a 3 keV cyclotron model from a 69 MG field.

unexplained by S+15. The new data allow us to study the origin of the secondary hump and test whether it could arise from accretion onto a second pole. We isolated an optical spectrum as follows. We obtained a spectrum of the orbital minimum, which occurs in the phase interval 0.31–0.37. We then subtracted it from the average spectrum in the phase interval 0.38–0.60. The difference spectrum shows modulations of the continuum also reminiscent of cyclotron harmonics but with much wider separation than those of the main pole (Fig. 11). They seem to be centred at $5.77 \times 10^{14} \text{ Hz}$ and $7.81 \times 10^{14} \text{ Hz}$, respectively, and could be identified with the third and fourth cyclotron harmonics. The identification is tentative, a model computation assuming a field of 69 MG, which is also shown in the figure gives some support for our interpretation but needs confirmation. If confirmed this measurement would give support to S+15’s hypothesis of a non-dipolar field structure.

An EPIC-*pn* spectrum was extracted for the phase interval 0.45–0.65. The hump spectrum was successfully fitted with a single temperature MEKAL model with a plasma temperature of order 4 keV between 0.2 and 5.0 keV. The result is shown in Fig. 12.

The X-ray flux of the secondary hump is an order of magnitude smaller than that of the bright phase, and its optical flux is approximately $1.4 \times 10^{-12} \text{ erg cm}^{-2} \text{ s}^{-1}$. The optical and X-ray spectra, together with the shape and phasing of the secondary hump in the light curve, reveal a secondary accretion region centred at phase ~ 0.58 , i.e. away from the mass-donating star. As observed in several other polars with a two-pole accretion geometry, for instance RX J1846.9+5538 (Schwarz et al. 2002), the weaker accreting pole has a significantly higher magnetic field strength. It is offset by only $\sim 140^\circ$ from the primary pole, which suggests a significantly off-centre WD magnetic field.

Since the secondary hump has duration $\Delta\phi_{\text{hump}} < 0.5$, it must be located in the WD’s southern hemisphere. Assuming a point-like emission region, the approximation for the colatitude

$$\beta = -\text{atan} \left[\frac{1}{\cos(\pi\Delta\phi) \tan i} \right] \quad (2)$$

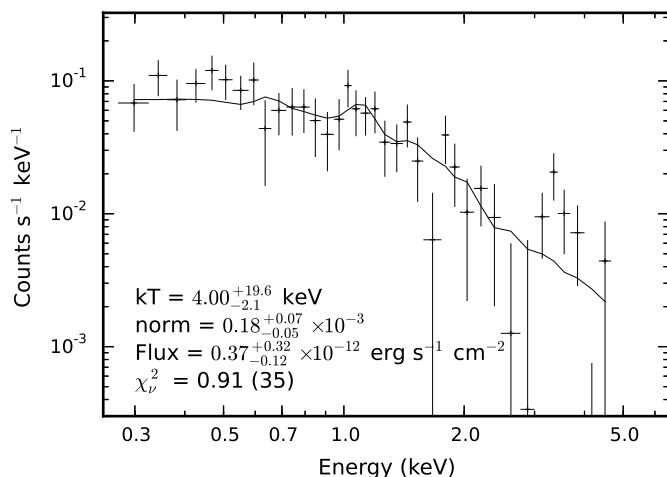


Fig. 12. EPIC-*pn* spectrum of the secondary hump ($0.45 < \phi < 0.65$) in Obs2, fitted with a single temperature MEKAL. The units of normalisation are the same as in Table 1.

is valid. From Fig. 6 we estimate the secondary hump to have $\Delta\phi_{\text{hump}} = 0.2 \pm 0.075$ and, given $i = 81.5^\circ \pm 2.2^\circ$ (S+15), we obtain colatitude $\beta_{\text{hump}} = 169^\circ \pm 5^\circ$. For high inclination i and small $\Delta\phi$, Eq. 2 is rather insensitive to changes in both, so our result is robust despite the difficulties in observing the second bright spot. The secondary bright spot is therefore likely to be a few degrees nearer the WD rotation axis than the primary bright spot ($\beta_{\text{bright}} \approx 18^\circ$).

3.5. Eclipse parameters

We used the OM data and X-ray data to derive eclipse timings for both observations. For the OM the times of ingress and egress were taken to be times of half-intensity, found using a semi-automated version of the “cursor” method described in Schwope & Thinius (2014) on 2 s binning. For the X-ray data, we simply used the times of the corresponding Bayesian Block change points. The results are summarised in Table 2. We did not use the OM data for the first and third eclipses in Obs1, because of data gaps. For the last eclipse in Obs2 did use MOS2 data because of the buffer overflow data gaps in the EPIC-*pn* data caused by the proton flare (Burwitz et al. 2004).

The eclipse centres in X-rays occur 3.4 ± 1.0 seconds earlier than predicted by the ephemeris in S+15, along with a smaller offset of 1.8 ± 0.5 s in the OM data. The eclipses may be slightly longer by 0.7 ± 0.5 and 1.1 ± 1.0 s in UV and X-rays, but the differences are not statistically significant. The differences in the timings may indicate that the X-ray and optical/UV emission do not arise from the same site in the accretion stream.

In Fig. 13 we show the phase-folded eclipse profiles in X-ray, UV, and STELLA optical wavelengths for both observations. No STELLA observations were available for Obs1. The X-ray and UV observations are binned into 2 s intervals, and the STELLA binning is 60 s. There is no indication that any of the eclipse ingresses or egresses are resolved at these bin sizes, suggesting that the emitting spot is less than 2 s in extent at UV and X-ray energies.

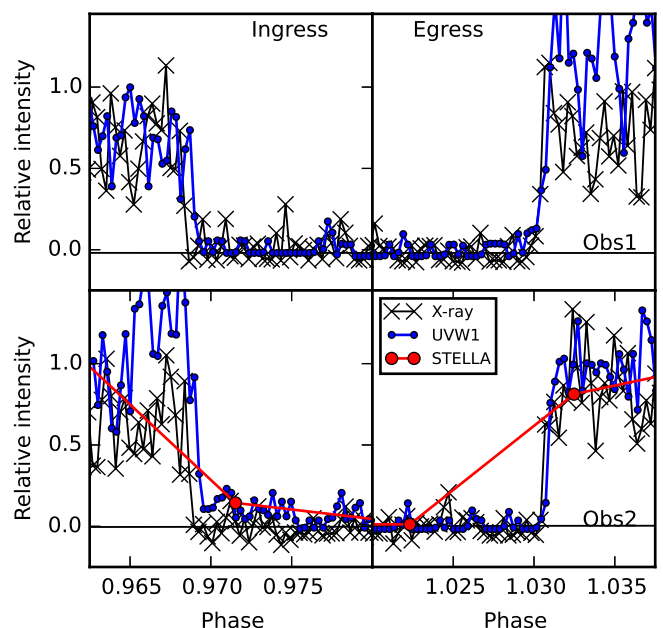


Fig. 13. Phase-folded eclipse profiles in EPIC-*pn* X-rays, UVW1, and STELLA optical wavelengths. The binning is 2 s for X-rays and UVW1, and 60 s in STELLA. The intensity is relative to the mean pre- and post-eclipse brightness. There is no evidence of an extended emitting spot at any wavelength.

3.6. The SED and the energy balance

According to the semi-empirical donor sequence of Knigge (2006, 2007), the 1.953-hour orbital period implies a secondary of spectral type M4.6. Combining the $M_V = 13.02$ and $M_B = 14.44$ absolute magnitudes for this spectral type with the observed $m_V \approx 21$ and $m_B \approx 22.4$ magnitudes during eclipse at low accretion rate, in Thorne et al. (2010) we obtained a distance to the system of about $D = 390$ pc. Assuming this distance and the MEKAL+*bbbodyrad* bright phase spectral model, then the total bright phase accretion luminosity $L_X = (\pi f_{\text{bb}} + 2\pi f_{\text{mekal}} + \pi f_{\text{cyc}})D^2$ was $> 3.9 \times 10^{31}$ and $\approx 6.8 \times 10^{31}$ erg s $^{-1}$ for the two observations. We conservatively set the accretion luminosity equal to the X-ray luminosity in Obs1 because we have no optical data to allow the cyclotron component to be measured. We infer accretion rates of 1.2×10^{-11} and $3 \times 10^{-11} M_\odot \text{ yr}^{-1}$. These values are similar to the intermediate accretion state of HU Aqr (Schwarz et al. 2009).

We attempted to determine whether J071126 was detectable during eclipse by counting source and weighted background photons between $0.975 < \phi < 1.025$ for all three instruments. In both observations the photon counts were consistent with zero, and we obtained 3σ upper limits of 0.03 photons per second in both observations. Assuming a MEKAL spectrum of temperature 1.0 keV, this puts an upper limit on the X-ray luminosity during eclipse of 6.7×10^{31} erg s $^{-1}$, or 4.55 times the bolometric luminosity of the secondary. Because the X-ray luminosity of the secondary is likely to be ~ 1000 times fainter, this result does not usefully constrain the luminosity of the parts of the accretion stream unobscured during eclipse.

The cyclotron spectral component lying in the optical and UV regime is clearly visible in our observations, as is the bremsstrahlung component in X-rays. A third feature caused by the absorption and re-radiation of some of the bremsstrahlung by the WD photosphere is expected as a blackbody-like bump at

Table 2. Timings of eclipse centres BJD(TDB) for *XMM-Newton* optical monitor and EPIC-*pn* instruments. To save space, the initial two digits (24) have been omitted from the timings. Offsets compared with the ephemeris of S+15 are given in seconds. The cycle numbers are given according to the ephemeris in S+15. For the last cycle of Obs2, we have used the EPIC-MOS2 data because of data interruptions in EPIC-*pn*. Weighted averages for eclipse offsets and durations are given in the final row.

Cycle	OM	Δt_{OM} (s)	Dur. (s)	EPIC- <i>pn</i>	Δt_{pn} (s)	Dur. (s)
14683	—			$56028.06349 \pm 2.1 \times 10^{-5}$	-6.2 ± 2.3	434.6 ± 3.6
14684	$56028.14491 \pm 1.3 \times 10^{-5}$	-2.7 ± 1.8	433.0 ± 2.2	$56028.14488 \pm 2.2 \times 10^{-5}$	-5.0 ± 2.4	433.8 ± 3.7
14685	—			$56028.22632 \pm 1.9 \times 10^{-5}$	0.1 ± 2.2	428.3 ± 3.3
14686	$56028.30766 \pm 7.4 \times 10^{-5}$	-3.0 ± 6.5	441.6 ± 12.7	$56028.30763 \pm 1.8 \times 10^{-5}$	-5.0 ± 2.1	433.9 ± 3.2
19145	$56391.16686 \pm 1.0 \times 10^{-5}$	-1.7 ± 1.8	434.2 ± 1.7	$56391.16686 \pm 1.0 \times 10^{-5}$	-2.5 ± 1.8	435.7 ± 1.7
19146	$56391.24826 \pm 1.9 \times 10^{-5}$	0.1 ± 2.3	434.0 ± 3.3	$56391.24820 \pm 1.0 \times 10^{-5}$	-5.6 ± 1.8	440.8 ± 1.7
19147	$56391.32961 \pm 1.7 \times 10^{-5}$	-2.3 ± 2.1	435.0 ± 2.9	$56391.32961 \pm 1.5 \times 10^{-5}$	-2.6 ± 2.0	435.8 ± 2.5
average	—	-1.8 ± 0.5	434.0 ± 0.5	—	-3.4 ± 0.9	434.4 ± 1.0

~ 20 – 50 eV (Cropper 1990), but the *XMM-Newton* observations do not extend to these low energies. The low energy blackbody component for Obs2 described in Table 1 is underluminous if it represents the re-emitted bremsstrahlung. We have attempted to place limits on an unobserved blackbody component for Obs2 lying in the hard UV/soft X-ray region in a manner similar to Ramsay & Cropper (2002).

The unobserved blackbody is subject to these restrictions: its emitting area can be no larger than the WD itself ($R_{bb} < 8000$ km), it can be no cooler than the WD ($T_{bb} > 0.64$ eV for a very cool polar primary; (Schmidt et al. 2005; Ferrario et al. 2015)), its energy density at UV wavelengths cannot exceed the OM observations, and it must not cause the X-ray spectral fits to deteriorate. We generated a series of blackbodies with temperatures and normalisations on a grid, with $0.75 \text{ eV} \leq T_{bb} \leq 50 \text{ eV}$ and $1 \text{ km} \leq R_{bb} \leq 8000 \text{ km}$, where we have expressed the normalisation as the radius of a sphere 390 pc away. We excluded trials in which the energy density exceeded the difference between bright and faint (excluding the secondary hump) phases in UV. We then fitted the Obs2 X-ray data between 200 eV and 1 keV with the MEKAL+*bbbodyrad* model of Table 1, replaced the original blackbody’s parameters with those of the grid, and rejected trials that caused the χ^2_ν to increase by more than 1. Finally, we compared the fluxes of the remaining trials to the flux in the MEKAL component. The results are shown in Fig 14. There is a small region of the parameter space in which a large soft excess could still exist. The cusp at $T_{bb} \approx 14.5$ eV, $R_{bb} \approx 2720$ km accommodates a very large soft blackbody component ($F_{bb} \approx 380 F_{\text{mekal}}$), but this region is only barely consistent with the X-ray and UV observations, and it is likely that better observations or more restrictive criteria would eliminate it.

For example, if it is assumed that all of the bright-phase UV flux is the reprocessed blackbody then the UVM2 eclipse ingresses and egresses (≤ 10 s; the low photon counts in the UVM2 filter do not allow as accurate a determination as in UVW1) limit its emitting area to a region no larger than 6% of the observer-facing WD hemisphere, represented by the dashed black line in Fig. 14. This does not intersect the blue region for cooler blackbodies, so in that area of parameter space, a significant portion of the UV flux must arise from something other than the blackbody (most likely the cyclotron component) and that would in turn push the lower edge of the blue region to smaller effective radii. The similarity of the UV and optical light curves suggests that most of the UV flux actually does come from cyclotron emission. Though not excluded entirely, a significant soft excess can only be concealed in a very restricted area of the parameter space.

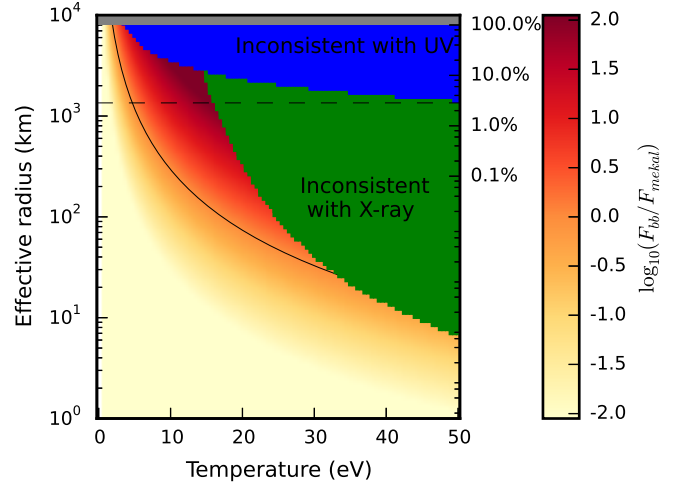


Fig. 14. Parameter space in which a soft excess can exist. The blue and green regions indicate areas excluded because they are not consistent with the *XMM-Newton* OM or X-ray observations, and the grey region indicates an emitting area larger than the 8000 km WD. Shaded points show the flux of the corresponding blackbody divided by the flux of the MEKAL component, and the black line tracks blackbodies with $F_{bb} = F_{\text{mekal}}$. The wedge-shaped region above the black line represents the area of the parameter space where a soft excess is still consistent with *XMM-Newton* observations. The dashed horizontal line represents a circular spot with an eclipse ingress time of 10 s, the largest still consistent with the UVM2 ingress. The right y-axis expresses the emitting area as a percentage of the WD surface.

4. Conclusions

We have performed a spectral and timing study of two *XMM-Newton* observations of the eclipsing polar J071126. The star was brighter in X-rays and UV in the second observation by a factor of approximately 2. J071126 has an X-ray hardness ratio of approximately 0.0–0.2 in the bright phase. These values are similar to those found for HU Aqr by Schwarz et al. (2009) (though calculated in slightly different energy bands), another point of similarity between these two systems.

There is some evidence that the X-ray eclipses may lead the optical and UV eclipses, suggesting that the X-ray plasma emission and cyclotron emission originate in different sites along the accretion arc. This view is supported by our finding that $F_{\text{cyc}} \approx 3 F_{\text{mekal}}$ for Obs2, hinting at a structured accretion region with parts being cyclotron-dominated (Beuermann 2004).

The longitude of the bright phase changes from a trailing spot during the lower accretion state to a leading one in the high accretion state. A similar effect was observed by S+15 but they caution that it could have been due to observing the system with different filters at different times. We can now rule out that explanation, because the *XMM-Newton* observations show the longitude shift occurring in X-rays and UV simultaneously.

A bright phase dip in optical wavelengths at $\phi \approx 0.80 - 0.85$ has been intermittently detected for this source and interpreted as partial obscuration of the accretion spot by the stream of accreting material (S+15). It has not been observed in the low accretion state but is usually detected in the intermediate and high states. The exception to this rule is the 2013 April observation by the STELLA telescope when, no dip was observed, despite being in the high state. Obs2 was nearly concurrent with them, and we see no evidence in UV of a bright phase dip, but obvious evidence for them in soft X-rays $\phi \approx 0.82$. This behaviour is puzzling at first glance. However, as pointed out by Watson et al. (1989, 1990) in a study of EF Eri, the dip in X-rays is due to photoelectric absorption, and in infrared/optical it is due to free-free absorption. These two processes scale the optical depth as N_H and N_H^2 respectively. Since we have found a dip column density ($N_H \lesssim 1.4 \times 10^{21} \text{ cm}^{-2}$) at least an order of magnitude lower than for EF Eri ($\sim 4 \times 10^{22} \text{ cm}^{-2}$) it follows that the bright phase dip ought to be two or more orders of magnitude less prominent for J071126 as for EF Eri.

Occurring just before eclipse ingress, the pre-eclipse dip is more perplexing. It implies that gas is lost from the accretion stream very near the limb of the companion. However, we found that the bright phase as a whole is consistent with zero or very low absorption, suggesting that a negligible amount of absorbing gas is lost from the accretion stream between the two regions responsible for the two dips. Further study will be necessary to understand the behaviour of both absorption dips.

The ROSAT X-ray observatory viewed the sky position of J071126 for a total exposure of 192 seconds during its All-Sky Survey campaign, but J071126 was not detected. If the system had been emitting as it was during the bright phases of Obs1 or Obs2, ROSAT would have detected it with count rates of 0.17 and 0.49 counts per second between 0.1 and 2.4 keV. These count rates would have easily been sufficient to put it in the ROSAT bright source catalogue (Voges et al. 1999). Given that the 192 seconds of exposure were accumulated over several scans that were separated by 96 min, it is implausible that the source could have escaped detection had it been in its high accretion state. We conclude that it was in a low state during the RASS. It is interesting to note that all ROSAT-discovered polars showed a pronounced soft blackbody-like radiation component, but bright polars without a prominent soft component have been discovered only in the *XMM-Newton* era. The underlying population of X-ray spectra will only be uncovered by the all-sky X-ray surveys with eROSITA, which will be more sensitive than ROSAT in its own spectral band by a factor of ~ 30 (Merloni et al. 2012; Schwope 2012).

The WD in J071126 probably accretes onto both poles during the high accretion state, because it shows a secondary bright phase in the UV and optical. The second bright spot is faint but visible in X-rays, and its X-ray spectrum is consistent with a cooling accretion plasma. Its optical spectra indicate a magnetic field twice as strong as the primary accretion spot, and it is not located directly opposite the main accreting pole, suggesting a highly non-dipolar field geometry. Complex magnetic field configurations seem to be common for polars (e.g. Beuermann et al. 2007). The secondary bright phase's position on the WD hemi-

sphere away from the mass-donor explains the low accretion rate but the trajectory used by matter to reach the remote pole is not known. Determining how it occurs will provide a better understanding of these systems.

Acknowledgements. We gratefully acknowledge support for this project by the German DLR under contract 50 OR 1405. This research made use of Astropy, a community-developed core Python package for Astronomy (Astropy Collaboration et al. 2013). We acknowledge with thanks the variable and comparison star observations from the AAVSO International Database contributed by observers worldwide and used in this research. This study is based partly on data obtained with the STELLA robotic telescope in Tenerife, an AIP facility jointly operated by AIP and IAC. This work made use of data collected at the Calar Alto observatory. We are grateful to the anonymous referee, whose comments improved the clarity of this work.

References

- Arnaud, K. A. 1996, in *Astronomical Society of the Pacific Conference Series*, Vol. 101, *Astronomical Data Analysis Software and Systems V*, ed. G. H. Jacoby & J. Barnes, 17
- Astropy Collaboration, Robitaille, T. P., Tollerud, E. J., et al. 2013, *A&A*, 558, A33
- Beuermann, K. 2004, in *Astronomical Society of the Pacific Conference Series*, Vol. 315, *IAU Colloq. 190: Magnetic Cataclysmic Variables*, ed. S. Vrielmann & M. Cropper, 187
- Beuermann, K., Euchner, F., Reinsch, K., Jordan, S., & Gänsicke, B. T. 2007, *A&A*, 463, 647
- Bilir, S., Karaali, S., & Tünel, S. 2005, *Astronomische Nachrichten*, 326, 321
- Burwitz, V., Haberl, F., Freyberg, M. J., et al. 2004, in *Society of Photo-Optical Instrumentation Engineers (SPIE) Conference Series*, Vol. 5165, *X-Ray and Gamma-Ray Instrumentation for Astronomy XIII*, ed. K. A. Flanagan & O. H. W. Siegmund, 123–130
- Burwitz, V., Reinsch, K., Schwope, A. D., et al. 1996, *A&A*, 305, 507
- Campbell, R. K., Harrison, T. E., Schwope, A. D., & Howell, S. B. 2008, *ApJ*, 672, 531
- Churazov, E., Gilfanov, M., Forman, W., & Jones, C. 1996, *ApJ*, 471, 673
- Cropper, M. 1990, *Space Sci. Rev.*, 54, 195
- Dorman, B. & Arnaud, K. A. 2001, in *Astronomical Society of the Pacific Conference Series*, Vol. 238, *Astronomical Data Analysis Software and Systems X*, ed. F. R. Harnden Jr., F. A. Primini, & H. E. Payne, 415
- Drake, A. J., Djorgovski, S. G., Mahabal, A., et al. 2009, *ApJ*, 696, 870
- Ezuka, H. & Ishida, M. 1999, *ApJS*, 120, 277
- Ferrario, L., de Martino, D., & Gänsicke, B. T. 2015, *Space Sci. Rev.*
- Gänsicke, B. T., Hoard, D. W., Beuermann, K., Sion, E. M., & Szkody, P. 1998, *A&A*, 338, 933
- Katysheva, N. & Shugarov, S. 2012, *Mem. Soc. Astron. Italiana*, 83, 670
- Kirsch, M. G. F., Altieri, B., Chen, B., et al. 2004a, in *Society of Photo-Optical Instrumentation Engineers (SPIE) Conference Series*, Vol. 5488, *UV and Gamma-Ray Space Telescope Systems*, ed. G. Hasinger & M. J. L. Turner, 103–114
- Kirsch, M. G. F., Becker, W., Benlloch-Garcia, S., et al. 2004b, in *Society of Photo-Optical Instrumentation Engineers (SPIE) Conference Series*, Vol. 5165, *X-Ray and Gamma-Ray Instrumentation for Astronomy XIII*, ed. K. A. Flanagan & O. H. W. Siegmund, 85–95
- Knigge, C. 2006, *MNRAS*, 373, 484
- Knigge, C. 2007, *MNRAS*, 382, 1982
- Liedahl, D. A., Osterheld, A. L., & Goldstein, W. H. 1995, *ApJ*, 438, L115
- Merloni, A., Predehl, P., Becker, W., et al. 2012, *ArXiv e-prints* [[arXiv:1209.3114](https://arxiv.org/abs/1209.3114)]
- Mewe, R., Gronenschild, E. H. B. M., & van den Oord, G. H. J. 1985, *A&AS*, 62, 197
- Qian, S.-B., Liu, L., Liao, W.-P., et al. 2011, *MNRAS*, 414, L16
- Ramsay, G. & Cropper, M. 2002, *MNRAS*, 335, 918
- Ramsay, G. & Cropper, M. 2004, *MNRAS*, 347, 497
- Scargle, J. D. 1998, *ApJ*, 504, 405
- Scargle, J. D., Norris, J. P., Jackson, B., & Chiang, J. 2013, *ApJ*, 764, 167
- Schmidt, G. D., Szkody, P., Vanlandingham, K. M., et al. 2005, *ApJ*, 630, 1037
- Schwarz, R., Greiner, J., Tovmassian, G. H., Zharikov, S. V., & Wenzel, W. 2002, *A&A*, 392, 505
- Schwarz, R., Schwope, A. D., Vogel, J., et al. 2009, *A&A*, 496, 833
- Schwope, A. 2012, *Mem. Soc. Astron. Italiana*, 83, 844
- Schwope, A. D., Beuermann, K., & Thomas, H.-C. 1990, *A&A*, 230, 120
- Schwope, A. D., Hambaryan, V., Schwarz, R., Kanbach, G., & Gänsicke, B. T. 2002, *A&A*, 392, 541
- Schwope, A. D., Mackebrandt, F., Thinius, B. D., et al. 2015, *Astronomische Nachrichten*, 336, 115

- Schwöpe, A. D., Schwarz, R., Sirk, M., & Howell, S. B. 2001, *A&A*, 375, 419
- Schwöpe, A. D. & Thinius, B. D. 2014, *Astronomische Nachrichten*, 335, 357
- Schwöpe, A. D., Thomas, H.-C., Mante, K.-H., Haefner, R., & Staude, A. 2003, *A&A*, 402, 201
- Strassmeier, K. G., Granzer, T., Weber, M., et al. 2004, *Astronomische Nachrichten*, 325, 527
- Templeton, M., Oksanen, A., Boyd, D., Pickard, R., & Maehara, H. 2009, *Central Bureau Electronic Telegrams*, 1652, 1
- Thorne, K., Garnavich, P., & Mohrig, K. 2010, *Information Bulletin on Variable Stars*, 5923, 1
- Voges, W., Aschenbach, B., Boller, T., et al. 1999, *A&A*, 349, 389
- Watson, M. G., Jameson, R. F., King, A. R., & Mason, K. O. 1990, in *Accretion-Powered Compact Binaries*, ed. C. W. Mauche, 283–288
- Watson, M. G., King, A. R., Jones, M. H., & Motch, C. 1989, *MNRAS*, 237, 299
- Worpel, H. & Schwöpe, A. D. 2015, *A&A*, 578, A80